Eclética Química Journal

Original Article

revista.iq.unesp.br

| Vol. 47 | n. 3 | 2022 |

Influence of structural disorder on the photocatalytic properties of ZnS nanocrystals prepared by the one-pot solvothermal approach

Victoria Gabriela Benatto[1], Guilherme da Silva Lopes Fabris[2,3], Julio Ricardo Sambrano[3], Carlton Anthony Taft[4], Felipe de Almeida La Porta[1,5+]

1. Federal University of Technology of Paraná, Laboratory of Nanotechnology and Computational Chemistry, Londrina, Brazil.
2. Federal University of Rio Grande do Norte, Department of Materials Engineering, Natal, Brazil.
3. São Paulo State University, Modeling and Molecular Simulation Group, Bauru, Brazil.
4. Brazilian Center of Physical Research, Rio de Janeiro, Brazil.
5. State University of Londrina, Post-Graduation Program in Chemistry, Londrina, Brazil.

+Corresponding author: Felipe de Almeida La Porta, **Phone**: +55 43 33159437, **Email address**: felipelaporta@utfpr.edu.br

ARTICLE INFO

Article history:
Received: October 04, 2021
Accepted: April 10, 2022
Published: July 01, 2022

Section Editor: Assis Vicente Benedetti

Keywords

1. ZnS
2. density functional theory
3. solvothermal processing
4. photocatalysis properties
5. electronic structure

ABSTRACT: This study focuses on the impact of the sulfur vacancies on the photocatalytic response of the ZnS nanocrystals synthesized by solvothermal method varying the concentration of zinc acetate/thiourea precursors. XRD patterns show that these samples have a hexagonal structure with different degrees of crystallinity, varying the crystallite size from 2.48 to 2.85 nm. The UV-Vis data reveals an absorption peak (at about 320 nm) characteristic of ZnS nanocrystals. As a result, a decrease in the bandgap value of these materials was observed from 3.78 to 3.62 eV. In principle, a comparison of these results and theoretical calculations reveals the formation of intermediate levels inside the bandgap due to structural polarization. These findings also corroborate the zeta potential measured for these samples, evidenced by an increase of positive charge of ZnS surfaces. Also, the low Miller-index surfaces, such as $(10\bar{1}0)$, $(11\bar{2}0)$ and (0001), were investigated by periodic density functional theory calculations, in nice agreement with the experimental data. A photocatalysis mechanism was investigated and confirmed the formation of reactive oxygen species.

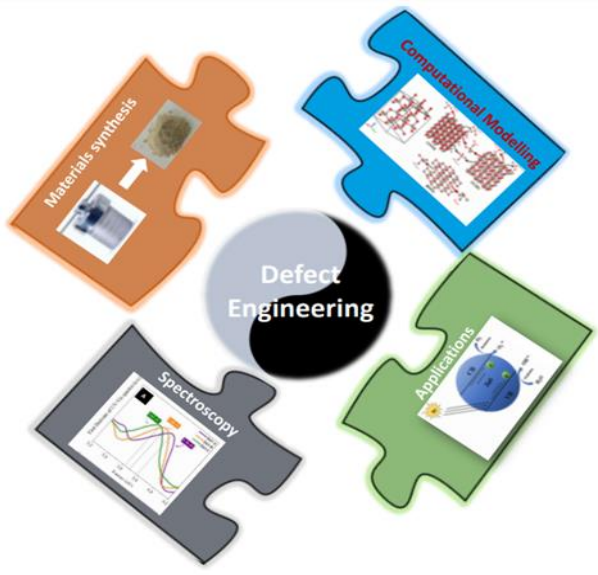

Eclética Química Journal, vol. 47, n. 3, 2022, 17-31
ISSN: 1678-4618
DOI: 10.26850/1678-4618eqj.v47.3.2022.p17-31

1. Introduction

In recent years, the contamination of water by micropollutants, especially organic dyes, has become a matter of serious environmental concern (Ayodhya and Veerabhadram, 2018; Bilal *et al.*, 2019; Byrne *et al.*, 2018). Additionally, recent studies have also shown a troubling detection of the novel coronavirus (denoted as SARS-CoV-2) in feces and sewage, raising the hypothesis of fecal-oral transmission (Heller *et al.*, 2020). To catalyze the decomposition reactions of these organic pollutants and pathogens, a wide variety of novel nanoscale semiconductor materials has attracted particular interest, because of their high photocatalytic efficiency in converting pollutants into environmentally friendly byproducts (Amorin *et al.*, 2019; Ayala-Durán *et al.*, 2020).

Among the materials proposed for this purpose, the zinc sulfide (ZnS) semiconductor materials have a wide bandgap of about 3.6 eV and exhibit highly tunable chemical and physical properties as well as unique functionalities for a huge variety of emerging technologies (Chen *et al.*, 2010; Hussain *et al.*, 2017; Ippen *et al.*, 2014; Jellison *et al.*, 1986; La Porta *et al.*, 2014a; Lee and Wu, 2017; Lin *et al.*, 2019; Sultana *et al.*, 2018; Xiao *et al.*, 2016; Zhang *et al.*, 2013; Ziegler *et al.*, 2008). A notable example of ZnS-related applications includes light-emitting diodes (LEDs), lasers, sensors, solar cells, piezoelectric nanogenerator, (photo)catalysis, and biomedical applications (Hussain *et al.*, 2017; Ippen *et al.*, 2014; Jellison *et al.*, 1986; La Porta *et al.*, 2014a; Lee and Wu, 2017; Lin *et al.*, 2019; Sultana *et al.*, 2018; X. Wang, *et al.*, 2011; Xiao *et al.*, 2016; Zhang *et al.*, 2013; Ziegler *et al.*, 2008). Furthermore, more recently, the ZnS-based heterostructure have been widely studied, mainly due to high quality of ZnS shell (in core/shell structures with a lower bandgap core) that contributes to an increase in the efficiency and stability of optoelectronic devices based on ZnS heterostructures (Chen *et al.*, 2021; Mukherjee and Selvaraj, 2021; Talapin *et al.*, 2004; P. Wang *et al.*, 2021).

Likely, due to their outstanding chemical and physical properties and incredible versatility, such nanocrystals have enormous importance in academic and industrial scenery. For this reason, several methodologies have been widely developed in the last decades for their simple and straightforward manufacture of ZnS-related materials with desired particle sizes, structures, compositions, and morphologies (Hussain *et al.*, 2017; Jellison *et al.*, 1986; Lee and Wu, 2017; Sultana *et al.*, 2018; X. Wang *et al.*, 2011; Xiao *et al.*, 2016; Zhang *et al.*, 2013). Nonetheless, among solution-based synthetic routes, it is known that the solvothermal approach is a relatively low-cost method and is widely used to produces diverse crystalline materials of high purity (La Porta *et al.*, 2014a; Li *et al.*, 2015; Santana *et al.*, 2011). Varela and coauthors have optimized the kinetics of solid-state reactions from hours to minutes, leading to obtaining spherical ZnS nanocrystals with controlled phase based on this strategy coupled with the use of microwave energy (La Porta *et al.*, 2013a; 2014a; b) Their work enabled a deep understanding of these ZnS crystals from a modern perspective based on the combination of theory, computational simulations, and experimental results aiming to elucidate these new nanoscale materials' physical and chemical behavior.

Therefore, this study is focused on the effects of structural defects caused by decreased concentration of zinc acetate/thiourea precursors in the solvothermal growth of ZnS nanocrystals with hexagonal structures for enhanced photocatalysis applications. Also, this study can significantly contribute to provide new chemical insights towards materials design with highly tailoring properties.

2. Experimental

2.1 Materials and synthesis

The ZnS nanocrystals with the hexagonal structure used in this study were synthesized from a one-pot solvothermal strategy based on a modification of the protocol established by Varela and collaborators (La Porta *et al.*, 2014a). Briefly, different concentrations of 1:1 zinc acetate/thiourea precursors system (such as 7.34 mmol for sample A, 3.68 mmol for sample B, or 1.835 mmol for sample C) were dissolved in approximately 50 mL of ethylene glycol. Then, 16 mmol of tetrabutylammonium hydroxide (40% wt/v) were added quickly and after 10 min the resulting reaction mixture was transferred into a Teflon-lined stainless-steel autoclave, properly sealed and then placed inside a muffle furnace for one-pot solvothermal synthesis at 160 °C for 120 min. After this period, the solvothermal system was slowly cooled and samples were collected near room temperature. Then, the precipitated powder was rinsed with deionized water/isopropanol several times in sequence and extracted by centrifugation, followed by room temperature drying for 24 h.

Eclética Química Journal, vol. 47, n. 3, 2022, 17-31
ISSN: 1678-4618
DOI: 10.26850/1678-4618eqj.v47.3.2022.p17-31

2.2 Characterization

The ZnS nanoparticles obtained were structurally characterized by X-ray diffraction (XRD) using a Bruker-D2 PHASER with Cu Kα radiation (λ = 1.5406 Å) in the 2θ range from 20 to 80° at 0.02° s^{-1}. For better reading and identification, the ZnS samples at the three different concentrations were named as A (7.34 mmol of zinc acetate/thiourea), B (3.67 mmol of zinc acetate/thiourea), and C (1.835 mmol zinc acetate/thiourea). Then, the UV-Vis spectra were recorded using a S60 Libra spectrophotometer (Biochrom), with a range of 190–1100 nm, using a quartz cuvette with a 10-mm optical path and two polished windows. Dynamic light scattering (DLS) analysis was performed using a Litesizer 500 particle size analyzer (ANTON PAAR), with 658 nm laser wavelength, using a 12.5 × 15.5 × 45 mm quartz cuvette. For these measurements, the powders (about 0.0005 g) were dispersed in 1 mL of water.

2.3 Photocatalytic degradation

The photocatalytic activity of spherical ZnS nanocrystals was evaluated in this study for the degraded methylene blue (MB) dye solution under ultraviolet C (UVC) lamps (15 W, G15T8/OF, OSRAM) at 254 nm irradiation. In a typical procedure, about 10 mg of the as-prepared catalyst was dispersed in 14 mL of 10 mg L^{-1} MB). In each test, the solution was continuously stirred for about of 20 min in the dark at room temperature (25 °C) in order to establish an adsorption-desorption equilibrium (Amorin *et al.*, 2019; Suzuki *et al.*, 2019a; 2021). During UVC irradiation, 1 mL of the solution was collected with an interval of 120 min. These MB dye solutions collected during degradation tests and then were analyzed at room temperature by a UV-Vis spectrometer (Biochrom).

2.4 Scavenger test

About 10 mg of catalyst in 14 mL of MB solution (10 mg L^{-1}) in the presence or not of different radical scavengers (in about 1 mmol), such as isopropanol (ISO), $AgNO_3$ (Ag), ammonium oxalate (AO), and pbenzoquinone (p-BQ), were added to the MB solution containing the photocatalyst (Pereira *et al.*, 2018; Suzuki *et al.*, 2021; Zhang *et al.*, 2012) and were mixed at a stirring rate of 300 rpm in the dark for 20 min. Later, the mixture was placed in the ultraviolet (UV) reactor at the same agitation rate. A 1 mL aliquot of the solution was collected after 120 min. The UV-Vis absorption spectra of the supernatant liquid were recorded using the same equipment as the previous experiment.

2.5 Computational simulation

The computational density functional theory (DFT) simulations were performed for the bulk ZnS and the $(10\bar{1}0)$, $(11\bar{2}0)$ and (0001) surfaces under periodic conditions as implemented in the CRYSTAL17 package (Dovesi *et al.*, 2017). Here, both the Zn and S atomic centers were described using the Triple-zetta Plus Polarization (TZVP) basis set, together with the B3LYP-D3 functional (Zhang *et al.*, 2012). The convergence criteria were controlled by a set of five thresholds (10-8, 10-8, 10-8, 10-8, 10-16) and for both Pack–Monkhorst and Gilat shrinking factor of 8. Also, tolerances were set to 0.0001 Hartree/bohr and 0.0004 bohr, respectively, to check on the gradient components as well as nuclear displacements (Dovesi *et al.*, 2017).

The surfaces with lower Miller index: $(10\bar{1}0)$, $(11\bar{2}0)$ and (0001) were simulated taking into account the stoichiometry/symmetry condition. Here, the surface energy (E_{surf}) was calculated as showed in Eq. 1:

$$E_{surf} = \frac{(E_{slab} - n \times E_{bulk})}{2} \quad (1)$$

where E_{slab} represent the total energy per unit cell of the slab in the (hkl) direction, E_{bulk} is defined as the total energy of the bulk per molecular unit, n is the number of surface layers and A is defined as the surface unit cell area (Dovesi *et al.*, 2017). In this case, the surfaces presented convergence in slab models from 8, 10 and 12 molecular units for the $(10\bar{1}0)$, $(11\bar{2}0)$ and (0001), respectively.

3. Results and discussion

As is well-known, the single-crystalline ZnS nanocrystals are usually required for many of their technological applications. Therefore, with that in mind, based on the solvothermal protocols developed by Varela and coauthors (La Porta *et al.*, 2013b; 2014a), this study has modified them to obtain single-crystalline ZnS spheric nanoparticles from the alteration of (zinc acetate/thiourea) precursor concentrations. Thus, the authors of this work have found that the variations in the (zinc acetate/thiourea) precursor concentrations lead to a different coloration for the prepared ZnS nanopowders, as shown in Fig. 1e–g. This important visual aspect reveals that this approach may, in

Eclética Química Journal, vol. 47, n. 3, 2022, 17-31
ISSN: 1678-4618
DOI: 10.26850/1678-4618eqj.v47.3.2022.p17-31

principle, indicate a possible increase in defects in the material, usually seen as a white/yellow colored powder and its darkening is likely due to the formation of sulfur vacancies in the ZnS prepared samples, which it can usually occur in three different load states (i.e., V_S^x, $V_S^{\bullet}$ and $V_S^{\bullet\bullet}$), and these cannot be distinguished. Hence, the darkening of the powder color indicates an increase in the density of sulfur vacancies, according to the decrease in the amount of precursor, which in turn can influence the photocatalytic properties of such materials significantly. In order to confirm these hypotheses, a structural analysis of these samples was performed. From the XRD pattern shown in Fig. 1a, it can be observed that ZnS crystals has a hexagonal structure (belongs to space group P63mc) as well as a high degree of crystallinity at the long-range (JCPDS #36–1450). No characteristic impurity peaks were observed in XRD data. Hence, this suggests that the products obtained have high purity. These results are in nice agreement with the work of Varela and coauthors (La Porta *et al.*, 2013b; 2014a). Figure 1b–d shows the average grain size and dispersion of sizes for these ZnS polycrystals which were determined from the XRD patterns. In particular, it can be assumed that these samples have a spherical crystallite as a model to XRD calculation of the grain size distribution, which is therefore based on using of a lognormal function. As a general result, these analyses suggest that such obtained powders have nanometric sizes.

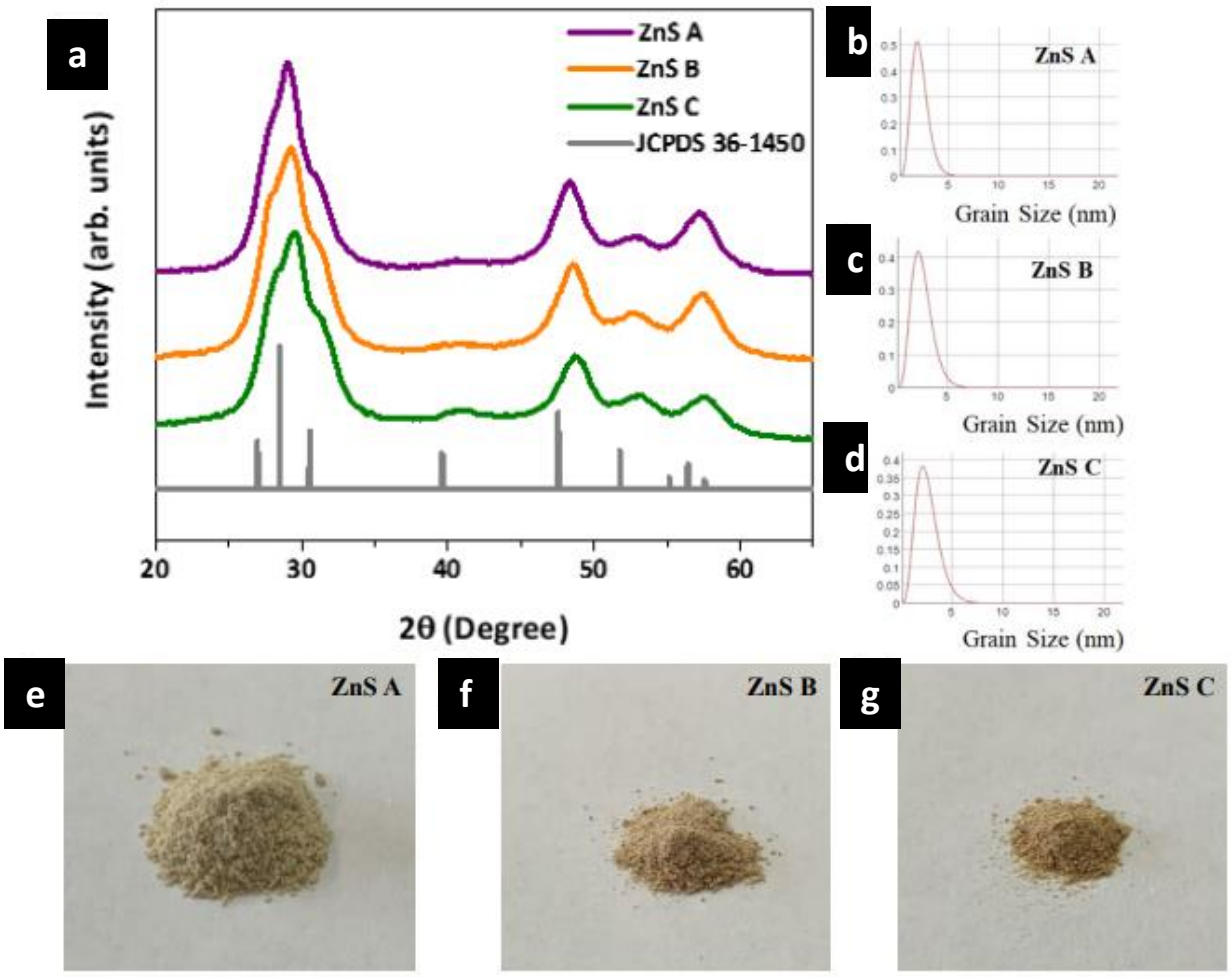

Figure 1. The XRD patterns, grain size distribution and digital photograph of powders. **(a)** XRD patterns of spheric ZnS nanoparticles; **(b-d)** Grain size distribution of ZnS samples, with grain sizes of about 2.6 nm, 3.1 nm, and 3.3 nm, for A, B and C samples; **(e-g)** Digital photograph of as-prepared ZnS nanopowders prepared using different (zinc acetate/thioureia) precursor concentrations in solvothermal conditions.

Moreover, another important aspect pertaining to the XRD peaks, as shown in Fig. 1a, reveals a significant widening due to the very small crystallite size, as well as a certain degree of amorphization of the samples may

Eclética Química Journal, vol. 47, n. 3, 2022, 17-31
ISSN: 1678-4618
DOI: 10.26850/1678-4618eqj.v47.3.2022.p17-31

indicate. Thus, from this perspective, the degree of crystallinity was determined for these prepared samples in this study (Tab. 1).

Table 1. Lattice parameters (*a*, *b* and *c*, in Å), crystallite size (nm), crystallinity (%), microstrain, theoretical band, gap energy (E_{gap}, in eV) and surface energy (E_{surf}, in J m^{-2}). For the (10$\bar{1}$0), (11$\bar{2}$0) and (0001) the *c* parameters are described by the thickness of the surface.

ZnS A				
Crystallite Size (nm)	Crystallinity (%)	Microstrain (ε)		
2.85	90.1	0.030		
Lattice parameters				
Plane	d_{hkl}	*a*	*c*	Unit cell volume (Å)
(100)	3.2786	3.7858	6.5571	93.9768
(002)	3.0686	3.5433	6.1371	77.0524
(101)	2.8832	3.3292	5.7663	63.9129
ZnS B				
Crystallite Size (nm)	Crystallinity (%)	Microstrain (ε)		
2.72	86.2	0.031		
Lattice parameters				
Plane	d_{hkl}	*a*	*c*	Unit cell volume (Å)
(100)	3.2786	3.7858	6.5571	93.9768
(002)	3.0538	3.5263	6.1077	75.9460
(101)	2.8832	3.3292	5.7664	63.9129
ZnS C				
Crystallite Size (nm)	Crystallinity (%)	Microstrain (ε)		
2.48	83.2	0.034		
Lattice parameters				
Plane	d_{hkl}	*a*	*c*	Unit cell volume (Å)
(100)	3.2786	3.7858	6.5571	93.9768
(002)	3.0408	3.5113	6.0817	74.9805
(101)	2.8588	3.3010	5.7176	62.3035

Models	**DFT**				
	a	*b*	*c*	E_{gap}	E_{surf}
Bulk	3.77	3.77	6.14	4.01	-
(10$\bar{1}$0)	3.77	6.15	17.78	3.88	1.07
(11$\bar{2}$0)	6.14	6.53	21.04	4.13	1.10
(0001)	3.77	3.77	8.87	4.47	1.61

However, based on the XRD data for a more accurate structural analysis we performed the peak deconvolution according to JCPDS #36–1450. Therefore, nine peaks are evident in the XRD pattern and were then deconvolution using a Voight function, as shown in Fig. 2a–c. After deconvolution of the XRD peaks, these results were analyzed and used to calculate the crystallite size, microstrain, interplanar distance, and lattice parameters for all prepared samples are summarized in Tab. 1. Here, the crystallite size for these samples as prepared was estimated by two methods. First, using the deconvoluted XRD peaks, the average crystallite size (*T*) was calculated by the Scherrer method (Eq. 2).

$$T = \frac{0.9\lambda}{\beta cos\theta} \quad (2)$$

where λ is defined as Cu Kα radiation; θ is defined as Bragg diffraction angle, and β is defined as peak width at half the maximum (FWHM) in radians (Guinier *et al.*, 1964). In this case, as the particles of ZnS have a spherical form the value of Scherrer constant is 0.9. Second, both the average strain and crystalline size of all prepared samples were then calculated using the

Eclética Química Journal, vol. 47, n. 3, 2022, 17-31
ISSN: 1678-4618
DOI: 10.26850/1678-4618eqj.v47.3.2022.p17-31

Williamson–Hall method (Eq. 3) (Suryanarayana, 1998). That is:

$$\frac{\beta\, cos\theta}{\lambda} = \frac{0.9}{T} + \frac{4\varepsilon\, sen\theta}{\lambda} \quad (3)$$

Here, FWHM can be expressed in terms of deformation (ε) which is determined by the slope of the straight line, and, in this case, T is determined by the intersection with the vertical axis, and the other parameters have the same meaning as in the Eq. 2 (Guinier *et al.*, 1964; La Porta *et al.*, 2014a; Suryanarayana, 1998). The Williamson–Hall plot for spheric ZnS nanocrystals as-prepared are here shown in Fig. 2d-f. In general, this trend observed in these Williamson–Hall results (negative slope) is due to the small crystallite size of about 3 nm obtained for these samples. This behavior has been explained in detail in a previous work (Suzuki *et al.*, 2019b).

Moreover, the interplanar spacing (d_{hkl}) is related to the ZnS lattice parameters a and c, from Eqs. 4 and 5:

$$2d_{hkl}sin\theta = n\lambda \quad (4)$$

$$\frac{1}{d^2} = \frac{4}{3}\left(\frac{h^2+hk+k^2}{a^2}\right) + \frac{l^2}{c^2} \quad (5)$$

Using the estimated values of interplanar distance, according to the above expression, the lattice parameters a and c were calculated by the following relation (Eq. 6):

$$a = \frac{\lambda}{\sqrt{3}sin\theta}, c = \frac{\lambda}{sin\theta} \quad (6)$$

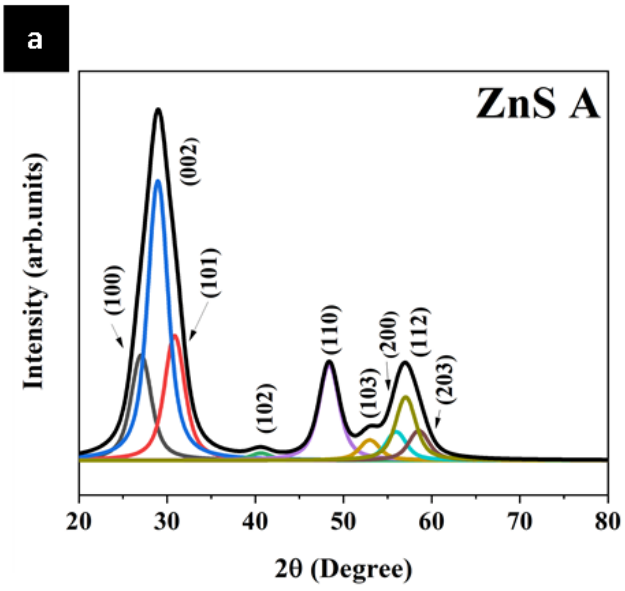

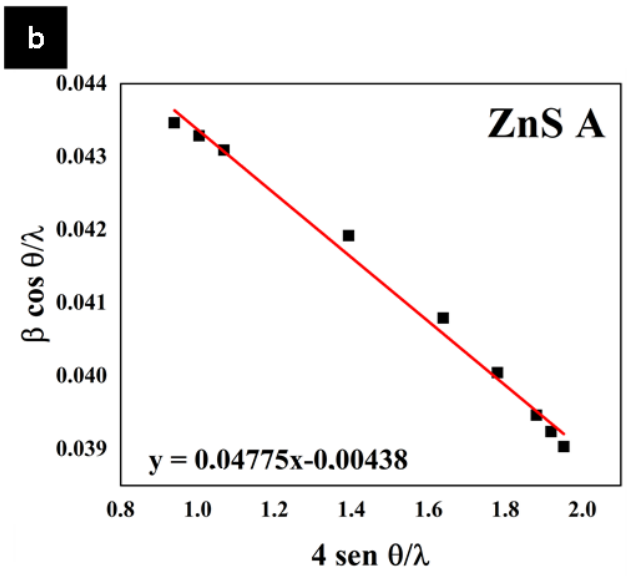

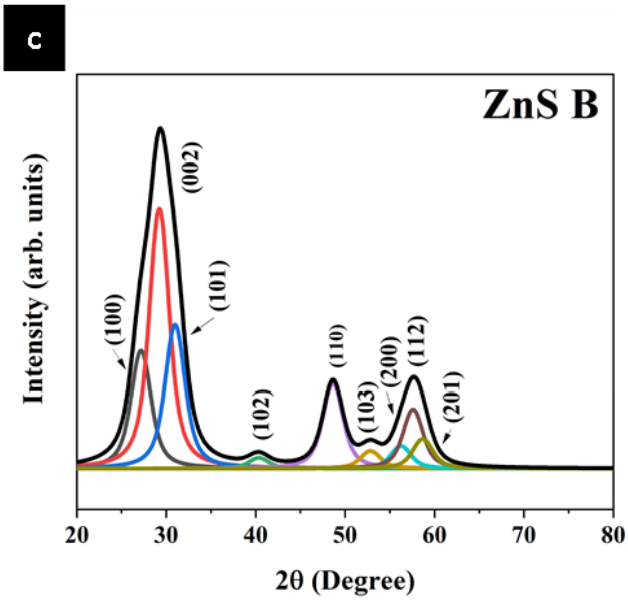

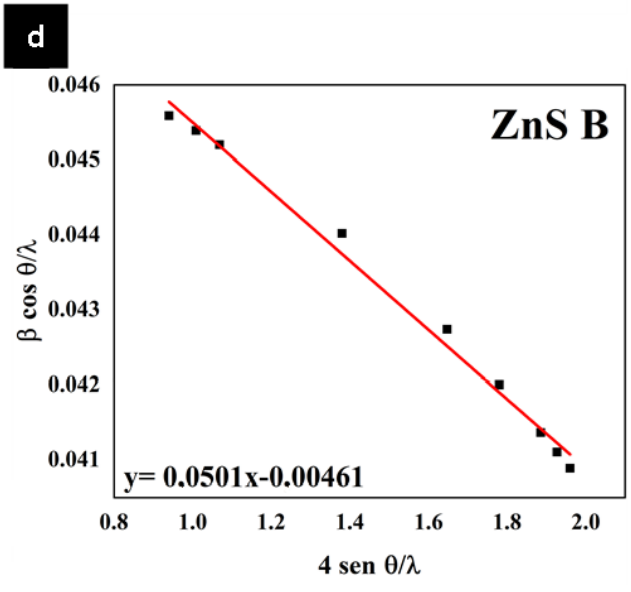

Eclética Química Journal, vol. 47, n. 3, 2022, 17-31
ISSN: 1678-4618
DOI: 10.26850/1678-4618eqj.v47.3.2022.p17-31

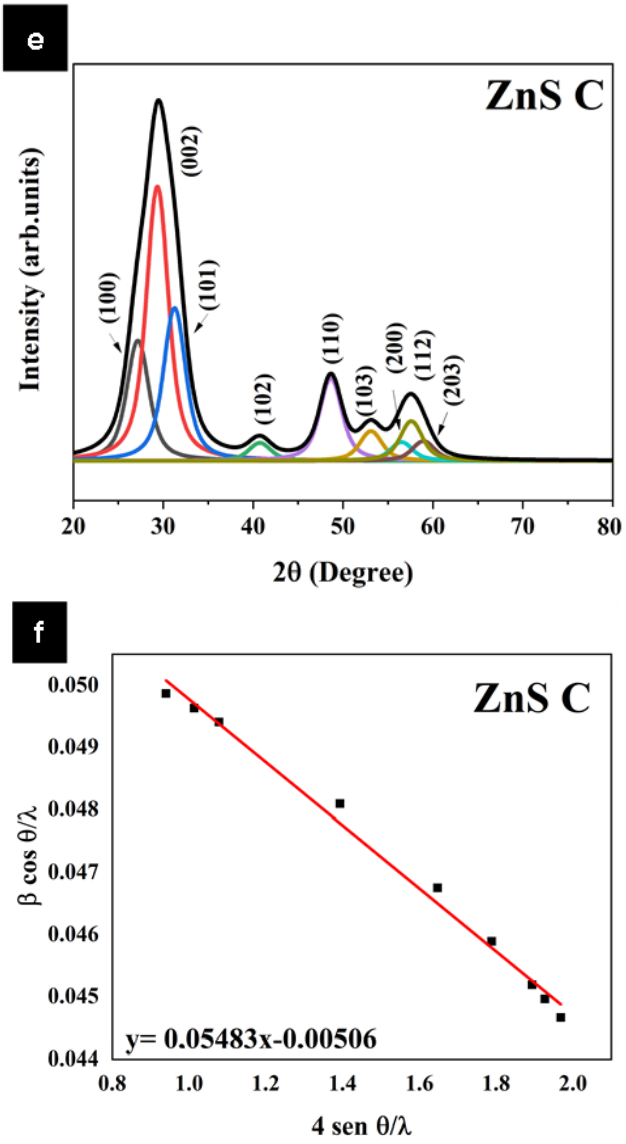

Figure 2. Deconvolution of XRD and Williamson–Hall analysis. **(a-c)** Deconvoluted XRD pattern into nine bands (according to JCPDS #36–1450); **(d-f)** Williamson–Hall analysis of the ZnS nanopowders.

As is well-known, the ZnS hexagonal structure (space group P63mc) is formed by tetragonal [ZnS_4] clusters as shown in Fig. 3a. As is well-known, the low-Miller index ($10\bar{1}0$), ($11\bar{2}0$) and (0001) surface planes, in general, are the most stable faces of hexagonal ZnS structure and hence are usually predominant in the obtained crystals, it has been extensively characterized from the diverse theoretical and experimental methodologies (Hamad *et al.*, 2002; La Porta *et al.*, 2017; Meng *et al.*, 2013). However, a more detailed analysis of clusters formed by the ($10\bar{1}0$), ($11\bar{2}0$) and (0001) surfaces show different atom arrangements as seen in Fig. 3. The surface modeling shows that for the ($10\bar{1}0$) and ($11\bar{2}0$), the outermost layers are mainly composed by [ZnS_3] clusters, as its inner layers are composed by [ZnS_4]; as well as the (0001) which is formed by [ZnS_4] clusters (Fig. 3). This leads to modulation of the catalytic activity in these crystal planes. In line with theoretical and experimental results, a decrease in cluster coordination of these exposed surfaces, particularly, contributes to an increase in surface energy, leading to a high chemical reactivity of these crystal planes (La Porta *et al.*, 2017; Huang *et al.*, 2012; Su *et al.*, 2014); however, as it can depend on the symmetry and between system planes, the results do not follow it perfectly. The surface energy of the (0001), ($10\bar{1}0$) and ($11\bar{2}0$) surfaces are shown in Tab. 1, in which the following stability order ($10\bar{1}0$) > ($11\bar{2}0$) > (0001) is shown. Even though the (0001) does not follow perfectly the rule, the ($10\bar{1}0$) is more favorable than the ($11\bar{2}0$) due to its lower concentration of [ZnS_3] in the exposed surface (La Porta *et al.*, 2017).

It is well-known that the UV-Vis absorption spectrum of colloidal semiconductor nanocrystals is size-dependent, as a direct consequence of the quantum confinement effect (El-Sayed, 2004; Jesus *et al.*, 2021; Talapin *et al.*, 2010). Figure 4a shows the first derivative UV–Vis absorption spectra of spheric ZnS nanocrystals, which were recorded after the powder sample being dispersed in water. For ZnS samples, it shows a red-shifted of the UV-Vis absorption peak at about 315, 317 and 323 nm, which is consistent with an increase in particle size and with the literature of ZnS (Yoffe, 2001). According to Calandra *et al.* (1999), the mathematical relation for the estimation of spherical diameter of the ZnS nanocrystals from the UV-Vis absorption peak is expressed as:

$$\lambda_{max} = 186.7 d_s^{0.13} \quad (7)$$

As expected from the following power law (Eq. 7), the spherical diameter values of samples A, B and C are, respectively, 55.9, 58.7 and 67.8 nm. Optical energies of the bandgap for these ZnS samples have been determined in this study by the analysis of their first derivative UV-Vis absorption curves according to a methodology discussed by Suzuki *et al.*, (2019a). As a result, the bandgap for the samples under study are shown in Tab. 1 and are in the range of 3.78 to 3.62 eV. In principle, a comparison of these results and theoretical calculations are also shown in Fig. 4c, reveals the formation of intermediate levels inside the bandgap due to structural polarization, as has been proposed by Varela and co-authors (La Porta *et al.*, 2013b; 2014a).

Eclética Química Journal, vol. 47, n. 3, 2022, 17-31
ISSN: 1678-4618
DOI: 10.26850/1678-4618eqj.v47.3.2022.p17-31

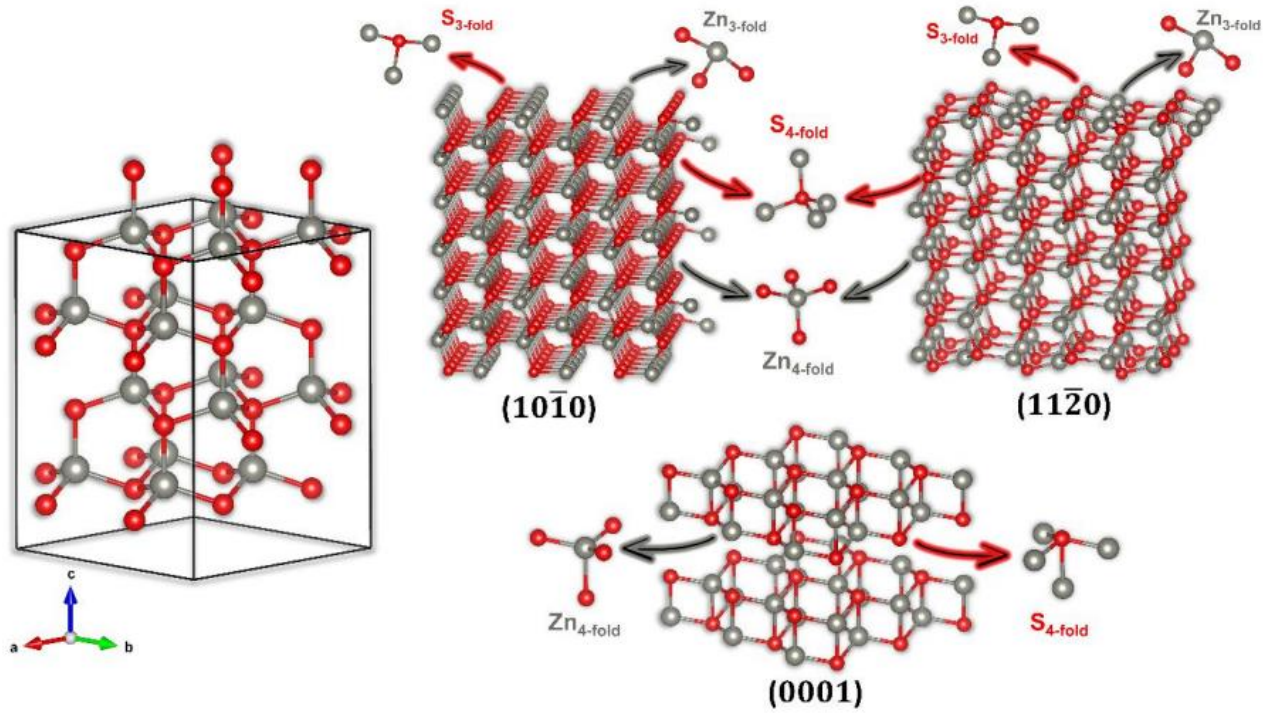

Figure 3. Illustration of the hexagonal ZnS unit cell and the cluster configurations for the (0001), (10$\bar{1}$0) and (11$\bar{2}$0) crystal planes.

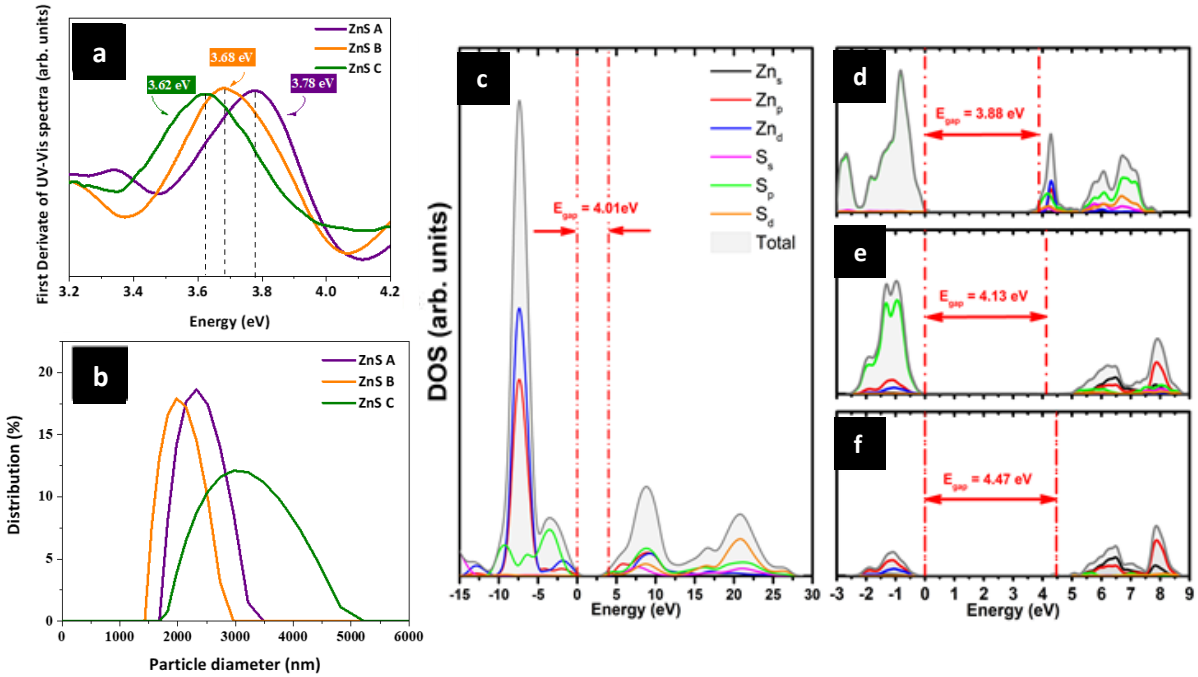

Figure 4. (a) First-derivative curves of the UV-Vis spectra. **(b)** DLS particle size analysis of the ZnS nanoparticles in water. Density of states of ZnS; **(c)** bulk; **(d)** (10$\bar{1}$0); **(e)** (11$\bar{2}$0); **(f)** (0001) surfaces.

Additionally, the projected density of states analysis for bulk ZnS model in Fig. 4c shows that the valence bands are mainly composed of sulfur 3p orbitals with a minor contribution of the zinc 3p orbitals, along with 3p and 4s zinc orbitals in the conduction band. From the ZnS surface models, it can be observed that the valence bands are quite similar to what was observed for the bulk, but in the conduction band the (10$\bar{1}$0) and (0001) has a major contribution of the zinc 4s orbital and a minor of zinc 3p orbital, but the (11$\bar{2}$0) has an equal

Eclética Química Journal, vol. 47, n. 3, 2022, 17-31
ISSN: 1678-4618
DOI: 10.26850/1678-4618eqj.v47.3.2022.p17-31

contribution of the zinc 4s and 3p orbitals with a minor contribution from the 3p from the sulfur (Fig. 4d and f).

Next, to complement the experimental results, the hydrodynamic diameter of the dispersed phase particles in solution was determined by DLS, in which the method is based on the analysis of light intensity fluctuations of light scattered by particles in the chaotic Brownian motion state (Lorber *et al.*, 2012; Stetefeld *et al.*, 2016). Figure 4b shows the hydrodynamic diameter values for the ZnS nanoparticles, dispersed in water. An analysis of the particle distribution obtained by the DLS suggests an increase in the size distribution with a decrease in the concentration of precursors, which is consistent with the UV-Vis results.

Also, the zeta potential of ZnS nanoparticles with varying concentrations of precursors was also measured on the same instrument, as shown in Fig. 5, which presents the stability characteristic of the system, for nanoparticles in solution by detecting the Doppler frequency change in scattered light because of particle motion (Kuznetsova *et al.*, 2016). As expected, an increase in the positive charge of ZnS nanocrystals was seen, which consists of the formation of sulfur vacancies. In addition, these results have agreed with the theoretical calculations.

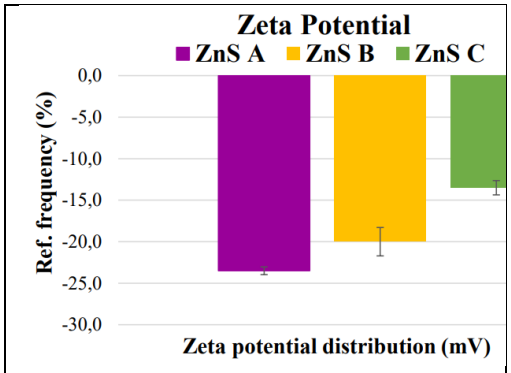

H_2O

Sample	HD (nm)	PDI (%)
A	3565	29.6
B	3616	27.4
C	4035	20.0

Figure 5. Zeta potential, hydrodynamic diameter (HD) and polydisposition index (PDI) of the ZnS nanoparticles.

The photocatalytic degradation of aqueous MB dye solution by ZnS samples was also investigated in this study (Fig. 6a–d). It is well-known that the photodegradation efficiency of the catalysts can, in principle, be fully adjusted through pseudo-first order reaction kinetics (Eq. 8):

$$In\left(\frac{C}{C_0}\right) = kt \quad (8)$$

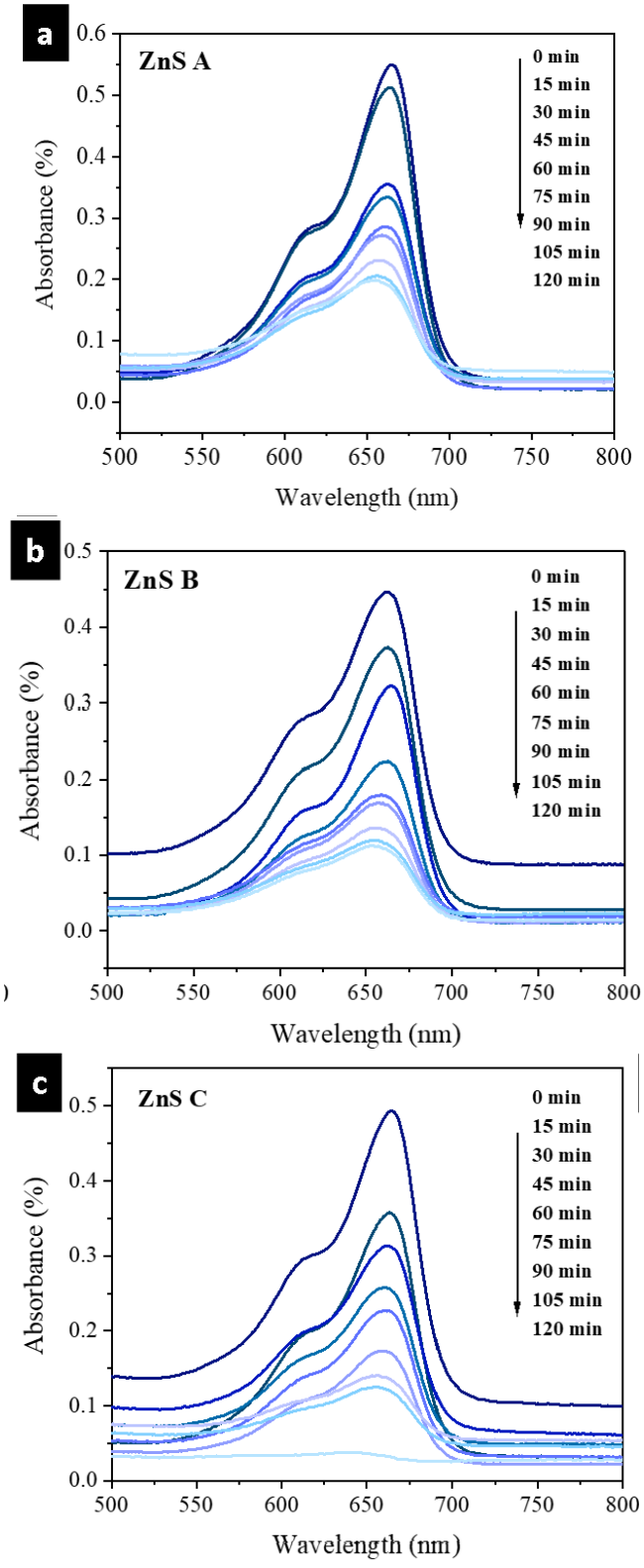

Eclética Química Journal, vol. 47, n. 3, 2022, 17-31
ISSN: 1678-4618
DOI: 10.26850/1678-4618eqj.v47.3.2022.p17-31

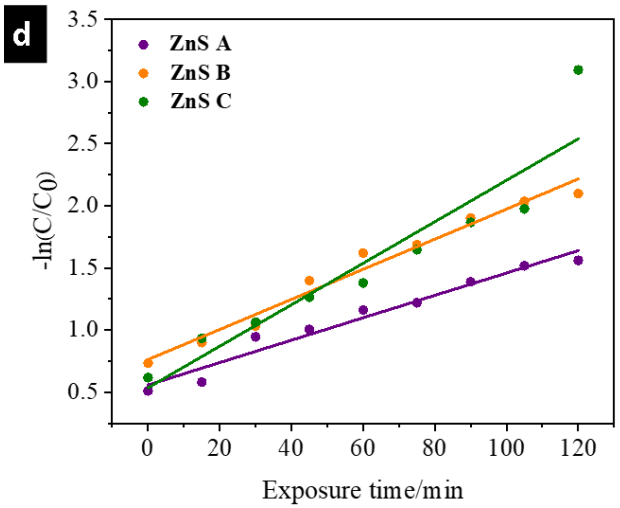

Figure 6. (a-c) UV-Vis absorption spectra of MB solutions at various irradiation times in the presence of the catalysts; **(d)** ln(C/C0) vs. degradation time.

As a result, it was observed that sample C is a better photocatalyst (k = 0.0115) than B (k = 0.0111) and A (k = 0.0082). This is due to the greater number of structural defects and sulfur vacancies on the ZnS samples, considerably favoring the adsorption of water (H_2O) and molecular oxygen (O_2) dissolved in MB solution. Thus, the following Eqs. 9–13, based on the Kröger–Vink notation (Chen *et al.*, 2015; Kröger and Vink, 1956; La Porta *et al.*, 2017; Sousa *et al.*, 2020), are used to explain the formation of the reactive oxygen species (ROS), which are usually responsible for degrading MB dye solution (Chen *et al.*, 2015; Pereira *et al.*, 2018; Su *et al.*, 2014).

$$[ZnS_4]^x + [ZnS_3.V_s^x] \rightarrow [ZnS_4]' + [ZnS_3.V_s^\bullet] \quad (9)$$

$$[ZnS_3.V_s^\bullet] + H_2O \rightarrow [ZnS_3.V_s^\bullet] \ldots OH_{2(ads)} \quad (10)$$

$$[ZnS_3.V_s^\bullet] \ldots OH_{2(ads)} \rightarrow [ZnS_3.V_s^x] \ldots OH^* + H^\bullet \quad (11)$$

$$[ZnS_3.V_s^\bullet] + O_2 \rightarrow [ZnS_3.V_s^\bullet] \ldots O_{2(ads)} \quad (12)$$

$$[ZnS_4]' + [ZnS_3.V_s^\bullet] \ldots O_{2(ads)} \rightarrow [ZnS_4]^x + [ZnS_3.V_s^\bullet] \ldots O_2' \quad (13)$$

It is well-known that photodegradation reactions are conducted by ROS (Chen *et al.*, 2015; Pereira *et al.*, 2018; Zhang *et al.*, 2012), as shown in the proposed mechanism above (Eqs. 9–13). Thus, with the specific purpose of confirming the formation of ROS, photodegradation tests were performed in the presence of different radical scavengers (Suzuki *et al.*, 2021). Figure 7 showed that the addition of AO, as a holes ($h^\bullet$) scavenger, did not cause significant changes in the photocatalytic degradation of the MB dye solution.

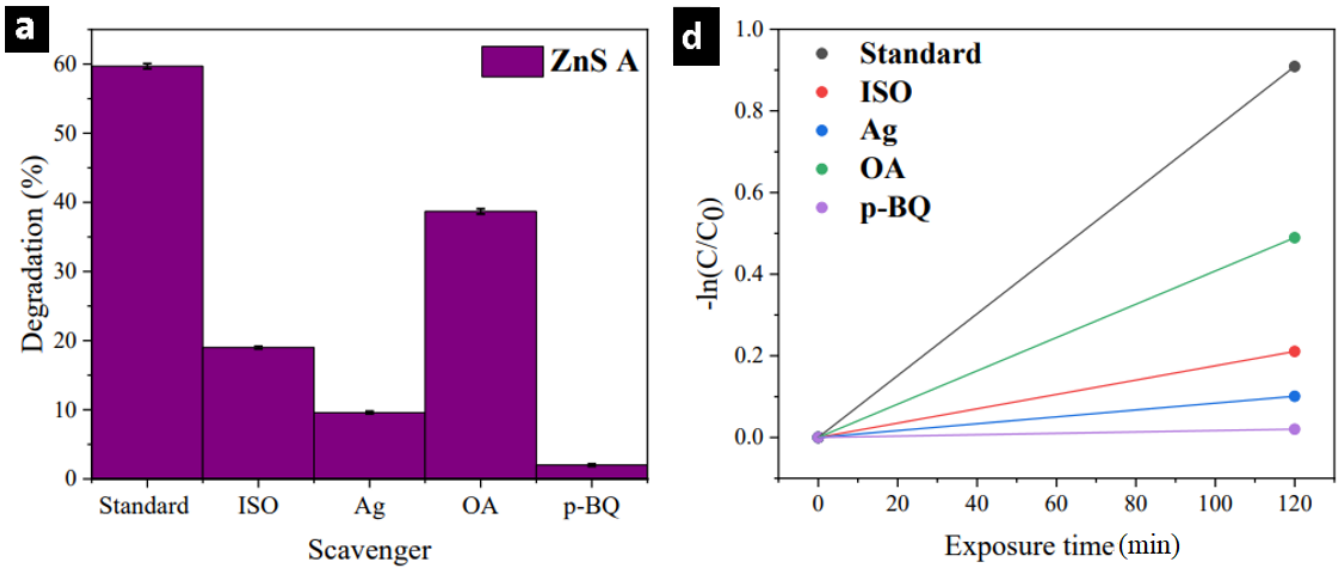

Eclética Química Journal, vol. 47, n. 3, 2022, 17-31
ISSN: 1678-4618
DOI: 10.26850/1678-4618eqj.v47.3.2022.p17-31

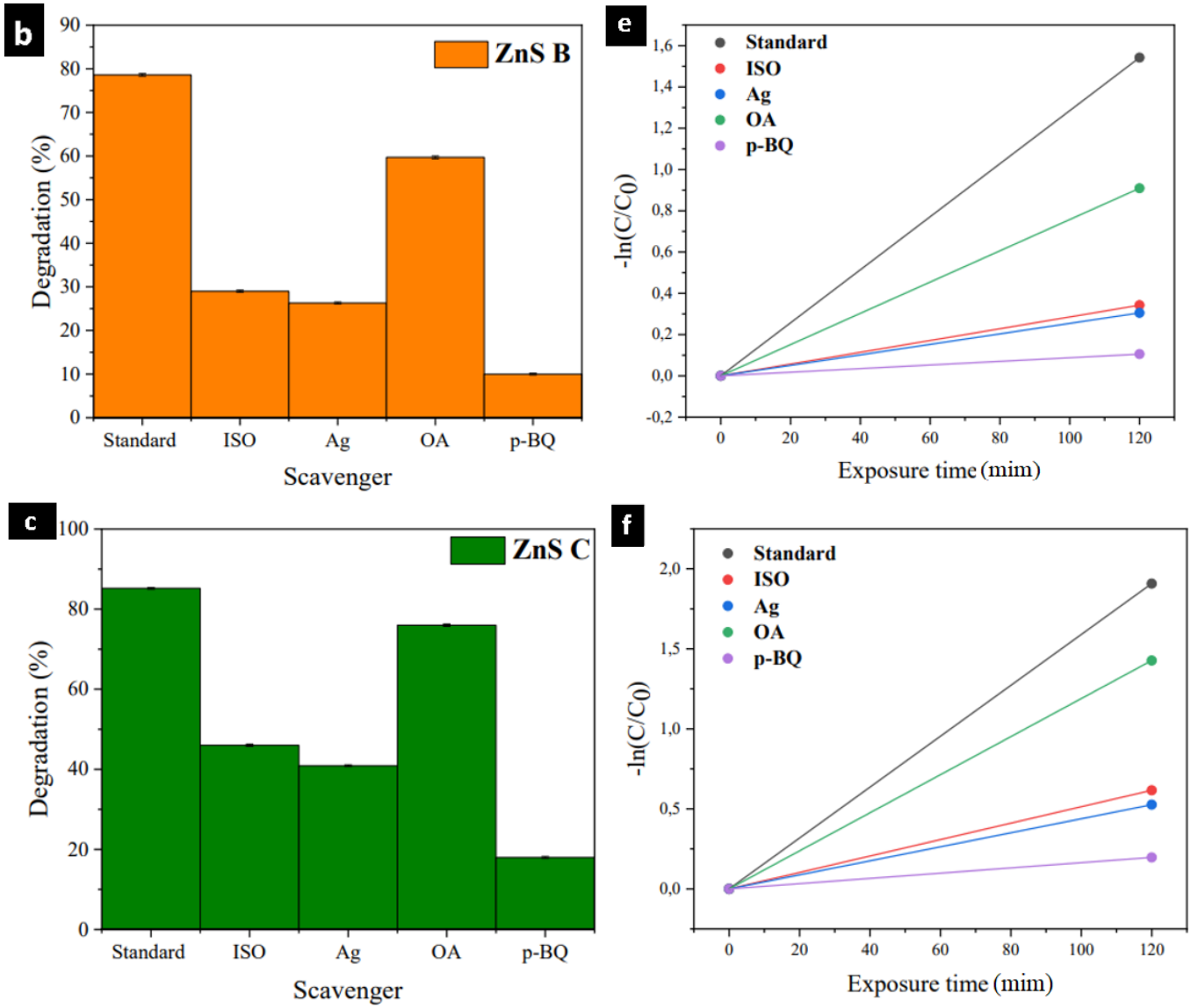

Figure 7. (a-c) Variation of degradation efficiency and **(d-f)** ln(C/C0) vs. degradation time for the ZnS samples in the presence of different scavengers.

In comparison, as illustrated in Fig. 7, it was found that the photodegradation of the MB dye solution is notably inhibited by the addition of ISO, Ag and p-BQ, which are reactive species such as radical species (OH*), electron (e') and superoxide radicals ($^{\bullet}O'_2$), indicating a more significant role to the photocatalytic mechanism. Photodegradation tests suggest that the high concentration of sulfur vacancies and structural defects significantly contribute to the adsorption of H_2O and O_2, improving the material's photocatalytic activity (Chen *et al.*, 2015; Liqiang *et al.*, 2006). Therefore, from this perspective, it can be assumed that these ROS are the active species responsible for leading to the complete degradation of the MB dye solution (Amorin *et al.*, 2019).

4. Conclusions

ZnS nanoparticles with different degrees of crystallinity were synthesized by the one-pot solvothermal method under different concentrations of zinc acetate/thiourea precursors. It was found from XRD patterns that the samples have a hexagonal structure, varying the crystallite size range from 2.48 to 2.85 nm. The DLS and UV-Vis measurements were also performed to analyze the particle size distribution and its optical properties. Overall, the results show the decrease in the concentration of precursors favors the formation of sulfur vacancies. Furthermore, bandgap engineering has a significant impact on the photocatalytic response of these samples. A

Eclética Química Journal, vol. 47, n. 3, 2022, 17-31
ISSN: 1678-4618
DOI: 10.26850/1678-4618eqj.v47.3.2022.p17-31

photocatalysis mechanism was investigated and confirmed the formation of ROS. Therefore, these complex defects are more effective sites for adsorption, leading to improved photocatalytic response. Studies are ongoing to assess the interaction of ZnS nanocrystals with the main protease of SARS-CoV-2.

Authors' contribution

Conceptualization: La Porta, F. A.
Data curation: Benatto, V. G.; Fabris, G. S. L.
Formal Analysis: Benatto, V. G.; Fabris, G. S. L.; La Porta, F. A.
Funding acquisition: La Porta, F. A.; Taft, C. A.; Sambrano, J. R.
Investigation: Benatto, V. G.; Fabris, G. S. L.
Methodology: Benatto, V. G.; Fabris, G. S. L.
Project administration: La Porta, F. A.; Taft, C. A.; Sambrano, J. R.
Resources: La Porta, F. A.; Taft, C. A.; Sambrano, J. R.
Software: Sambrano, J. R.; Fabris, G. S. L.
Supervision: La Porta, F. A.; Taft, C. A.; Sambrano, J. R.
Validation: Benatto, V. G.; Fabris, G. S. L.
Visualization: Benatto, V. G.; Fabris, G. S. L.
Writing – original draft: Benatto, V. G.; Fabris, G. S. L.
Writing – review & editing: La Porta, F. A.; Taft, C. A.; Sambrano, J. R.

Data availability statement

The data will be available upon request.

Funding

Fundação de Amparo à Pesquisa do Estado de São Paulo (FAPESP). Grant No: 2019/08928-9; 2013/07296-2.

Conselho Nacional de Desenvolvimento Científico e Tecnológico (CNPq). Grant No: 304604/2018-6; 307213/2021-8.

Coordenação de Aperfeiçoamento de Pessoal de Nível Superior (CAPES). Finance Code 001; Grant No: 88887.467334/2019-00.

Molecular Simulations Laboratory (São Paulo State University, Bauru, Brazil).

Acknowledgments

The deceased Prof. Dr. J. A. Varela (São Paulo State University, Brazil) did the research for decades with advanced ceramics, in collaboration with other experimental/theoretical groups, leaving a very important legacy still used by many groups in their work today. This research paper is dedicated to his memory.

References

Amorin, L. H.; Suzuki, V. Y.; Paula, N. H.; Duarte, J. L.; Silva, M. A. T, Taft, C. A.; La Porta, F. A. Electronic, structural, optical, and photocatalytic properties of graphitic carbon nitride. *New J. Chem.* **2019**, *43* (34), 13647–13653. https://doi.org/10.1039/C9NJ02702E

Ayala-Durán, S. C.; Hammer, P.; Nogueira, R. F. P. Surface composition and catalytic activity of an iron mining residue for simultaneous degradation of sulfonamide antibiotics. *Environ. Sci. Pollut. Res.* **2020**, *27*, 1710-1720. https://doi.org/10.1007/s11356-019-06662-1

Ayodhya, D.; Veerabhadram, G. A review on recent advances in photodegradation of dyes using doped and heterojunction based semiconductor metal sulfide nanostructures for environmental protection. *Mater. Today Energy* **2018**, *9*, 83-113. https://doi.org/10.1016/j.mtener.2018.05.007

Bilal, M.; Adeel, M.; Rasheed, T.; Zhao, Y.; Iqbal, H. M. N. Emerging contaminants of high concern and their enzyme-assisted biodegradation - A review. *Environ. Int.* **2019**, *124*, 336-353. https://doi.org/10.1016/j.envint.2019.01.011

Byrne, C.; Subramanian, G.; Pillai, S. C. Recent advances in photocatalysis for environmental applications. *J. Environ. Chem. Eng.* **2018**, *6*, 3531-3555. https://doi.org/10.1016/j.jece.2017.07.080

Calandra, P.; Goffredi, M.; Liveri, V. T. Study of the growth of ZnS nanoparticles in water/AOT/nheptane microemulsions by UV-absorption spectroscopy. *Colloids Surfaces A Physicochem. Eng. Asp.* **1999**, *160*, 9-13. https://doi.org/10.1016/S0927-7757(99)00256-3

Chen, D.; Huang, F.; Ren, G.; Li, D.; Zheng, M.; Wang, Y.; Lin, Z. ZnS nano-architectures: Photocatalysis, deactivation and regeneration. *Nanoscale* **2010**, *2*, 2062-2064. https://doi.org/10.1039/c0nr00171f

Chen, S.; Shen, S.; Liu, G.; Qi, Y.; Zhang, F.; Li, C. Interface engineering of a CoOx/Ta3N5 photocatalyst for unprecedented water oxidation performance under visible-light- Irradiation. *Angew. Chemie - Int. Ed.* **2015**, *54*, 3047-3051. https://doi.org/10.1002/anie.201409906

Chen, K.; Tang, W.; Chen, Y.; Yuan, R.; Lv, Y.; Shan, W.; Zhang, W. H. A facile solution processed ZnO@ZnS core-

shell nanorods arrays for high-efficiency perovskite solar cells with boosted stability. *J. Energy Chem.* **2021**, *61*, 553-560. https://doi.org/10.1016/j.jechem.2021.02.018

Dovesi, R.; Saunders, V. R.; Roetti, C.; Orlando, R.; Zicovich-Wilson, C. M.; Pascale, F.; Civalleri, B.; Doll, K.; Harrison, N. M.; Bush, I. J.; D'Arco, P.; Llunell, M.; Causà, M.; Noël, Y.; Maschio, L.; Erba, A.; Rerat, M.; Casassa, S. C. CRYSTAL17 User's Manual. Univ. Torino, Torino (2017).

El-Sayed, M. A. Small Is Different: Shape-, Size-, and Composition-Dependent Properties of Some Colloidal Semiconductor Nanocrystals. *Acc. Chem. Res.* **2004**, *37* (5), 326-333. https://doi.org/10.1021/ar020204f

Guinier, A., Lorrain, P., Lorrain, D. S.; Gillis, J. X-Ray Diffraction in Crystals, Imperfect Crystals, and Amorphous Bodies. *Phys. Today* **1964**, *17*, 70-72. https://doi.org/10.1063/1.3051547

Hamad, S.; Cristol, S.; Catlow, C. R. A. Surface structures and crystal morphology of ZnS: Computational study. *J. Phys. Chem. B* **2002**, *106*, 11002-11008. https://doi.org/10.1021/jp026396d

Heller, L.; Mota, C. R.; Greco, D. B. COVID-19 faecal-oral transmission: Are we asking the right questions? *Sci. Total Environ.* **2020,** *729*, 138919. https://doi.org/10.1016/j.scitotenv.2020.138919

Huang, W. C.; Lyu, L. M.; Yang, Y. C.; Huang, M. H. Synthesis of Cu 2O nanocrystals from cubic to rhombic dodecahedral structures and their comparative photocatalytic activity. *J. Am. Chem. Soc.* **2012**, *134*, 1261- 1267. https://doi.org/10.1021/ja209662v

Hussain, S.; Liu, T.; Javed, M. S.; Aslam, N.; Zeng, W. Highly reactive 0D ZnS nanospheres and nanoparticles for formaldehyde gas-sensing properties. *Sens. Actuators B Chem.* **2017**, *239*, 1243-1250. https://doi.org/10.1016/j.snb.2016.09.128

Ippen, C.; Greco, T.; Kim, Y.; Kim, J.; Suk, M.; Jong, C.; Wedel, A. ZnSe / ZnS quantum dots as emitting material in blue QD-LEDs with narrow emission peak and wavelength tunability. *Org. Electron.* **2014**, *15*, 126-131. https://doi.org/10.1016/j.orgel.2013.11.003

Jellison, G. E.; Wood, R. F. Antireflection coatings for planar silicon solar cells. *Solar Cells* **1986**, *18*, 93-114. https://doi.org/10.1016/0379-6787(86)90029-3

Jesus, J. P. A.; Jimenez, M. Z.; La Porta, F. de A. Theoretical investigation on the effects of electric field on the electronic structure and spectroscopic properties of Zn6−xCdxS6 clusters as model systems of semiconductor quantum dots. *Comput. Mater. Sci.* **2021**, *188*, 110147. https://doi.org/10.1016/j.commatsci.2020.110147

Kröger, F. A.; Vink, H. J. Relations between the Concentrations of Imperfections in Crystalline Solids. *Solid State Phys.* **1956**, *3*, 307-435. https://doi.org/10.1016/S0081-1947(08)60135-6

Kuznetsova, Y. V.; Kazantseva, A. A.; Rempel, A. A. Zeta Potential, Size, and Semiconductor Properties of Zinc Sulfide Nanoparticles in a Stable Aqueous Colloid Solution. Russ. *J. Phys. Chem. A* **2016**, *90*, 864-869. https://doi.org/10.1134/S0036024416040154

La Porta, F. A.; Ferrer, M. M.;Santana, Y. V. B.; Raubach, C. W.; Longo, V. M.; Sambrano, J. R.; Longo, E.; Andrés, J.; Li, M. S.; Varela, J. A. Towards an Understanding on the Role of Precursor in the Synthesis of ZnS Nanostructures. Curr. Phys. Chem. **2013a**, *3*(4), 378-385. https://doi.org/10.2174/18779468113036660012

La Porta, F. A.; Ferrer, M. M.; De Santana, Y. V. B.; Raubach, C. W.; Longo, V. M.; Sambrano, J. R.; Longo, E.; Andrés, J.; Li, M. S.; Varela, J. A. Synthesis of Wurtzite ZnS Nanoparticles Using the Microwave Assisted Solvothermal Method. *J. Alloys Compd.* **2013b**, *556*, 153-159. https://doi.org/10.1016/j.jallcom.2012.12.081

La Porta, F. A.; Andrés, J.; Li, M. S.; Sambrano, J. R.; Varela, J. A.; Longo, E. Zinc Blende versus Wurtzite ZnS Nanoparticles: Control of the Phase and Optical Properties by Tetrabutylammonium Hydroxide. *Phys. Chem. Chem. Phys.* **2014a**, *16* (37), 20127-20137. https://doi.org/10.1039/C4CP02611J

La Porta, F. A.; Gracia, L.; Andrés, J.; Sambrano, J. R.; Varela, J. A.; Longo, E. A DFT Study of Structural and Electronic Properties of ZnS Polymorphs and Its Pressure-Induced Phase Transitions. *J. Am. Ceram. Soc.* **2014b**, *97* (12), 4011-4018. https://doi.org/10.1111/jace.13191

La Porta, F. A.; Nogueira, A. E.; Gracia, L.; Pereira, W. S.; Botelho, G.; Mulinari, T. A.; Andrés, J.; Longo, E. An Experimental and Theoretical Investigation on the Optical and Photocatalytic Properties of ZnS Nanoparticles. *J. Phys. Chem. Solids* **2017**, *103*, 179-189. https://doi.org/10.1016/j.jpcs.2016.12.025

Lee, G.; Wu, J. J. Recent developments in ZnS photocatalysts from synthesis to photocatalytic applications - A review. *Powder Technol.* **2017**, *318*, 8-22. https://doi.org/10.1016/j.powtec.2017.05.022

Li, J.; Wu, Q.; Wu, J. Synthesis of Nanoparticles via Solvothermal and Hydrothermal Methods. In: Aliofkhazraei, M. (eds) Handbook of Nanoparticles. Springer, Cham., **2016**, 265-293. https://doi.org/10.1007/978-3-319-15338-4

Lin, Z. Q.; Wang, G. G.; Li, L. H.; Wang, H.; Tian, J. L.; Zhang, H. Y.; Han, J. C. Preparation and Protection of ZnS Surface Sub-Wavelength Structure for Infrared Window. *Appl. Surf. Sci.* **2019**, *470*, 395-404.

Eclética Química Journal, vol. 47, n. 3, 2022, 17-31
ISSN: 1678-4618
DOI: 10.26850/1678-4618eqj.v47.3.2022.p17-31

https://doi.org/10.1016/j.apsusc.2018.11.156

Liqiang, J.; Yichun, Q.; Baiqi, W.; Shudan, L.; Baojiang, J.; Libin, Y.; Wei, F.; Honggang, F.; Jiazhong, S. Review of photoluminescence performance of nano-sized semiconductor materials and its relationships with photocatalytic activity. *Sol. Energy Mater. Sol. Cells* **2006**, *90*, 1773-1787. https://doi.org/10.1016/j.solmat.2005.11.007

Lorber, B.; Fischer, F.; Bailly, M.; Roy, H.; Kern, D. Protein analysis by dynamic light scattering: Methods and techniques for students. *Biochem. Mol. Biol. Educ.* **2012**, *40*, 372-382. https://doi.org/10.1002/bmb.20644

Meng, X.; Xiao, H.; Wen, X.; Goddard, W. A.; Li, S.; Qin, G. Dependence on the structure and surface polarity of ZnS photocatalytic activities of water splitting: First-principles calculations. *Phys. Chem. Chem. Phys.* **2013**, *15*, 9531-9539. https://doi.org/10.1039/c3cp50330e

Mukherjee, S.; Selvaraj, J.; Paramasivam, T. Ag-Doped ZnInS/ZnS Core/Shell Quantum Dots for Display Applications. *ACS Appl. Nano Mater.* **2021**, *4*, 10228-10243. https://doi.org/10.1021/acsanm.1c01720

Pereira, W. da S.; Sczancoski, J. C.; Calderon, Y. N. C.; Mastelaro, V. R.; Botelho, G.; Machado, T. R.; Leite, E. R.; Longo, E. Influence of Cu substitution on the structural ordering, photocatalytic activity and photoluminescence emission of Ag 3-2x Cu x PO 4 powders. *Appl. Surf. Sci.* **2018**, *440*, 61-72. https://doi.org/10.1016/j.apsusc.2017.12.202

Santana, Y. V. B.; Raubach, C. W.; Ferrer, M. M.; La Porta, F. A.; Sambrano, J. R.; Longo, V. M.; Leite, E. R.; Longo, E. Experimental and theoretical studies on the enhanced photoluminescence activity of zinc sulfide with a capping agent. J. Appl. Phys. **2011**, *110*, 123507. https://doi.org/10.1063/1.3666070

Sousa, G. S.; Nobre, F. X.; Araújo Júnior, E. A.; Sambrano, J. R.; Albuquerque, A. dos R.; Bindá, R. dos S.; Couceiro, P. R. da C.; Brito, W. R.; Cavalcante, L. S.; Santos, M. R. de M. C.; Matos, J. M. E. Hydrothermal synthesis, structural characterization and photocatalytic properties of β-Ag2MoO4 microcrystals: Correlation between experimental and theoretical data. *Arab. J. Chem.* **2020**, *13*, 2806-2825. https://doi.org/10.1016/j.arabjc.2018.07.011

Stetefeld, J.; McKenna, S. A.; Patel, T. R. Dynamic light scattering: a practical guide and applications in biomedical sciences. *Biophys. Rev.* **2016**, *8*, 409-427. https://doi.org/10.1007/s12551-016-0218-6

Su, D.; Dou, S.; Wang, G. Single crystalline Co3O4 nanocrystals exposed with different crystal planes for Li-o2 batteries. *Sci. Rep.* **2014**, *4*, 5767. https://doi.org/10.1038/srep05767

Sultana, A.; Middya, T. R.; Mandal, D. ZnS-paper based flexible piezoelectric nanogenerator. *AIP Conf. Proc.* **2018**, *1942*, 120018. https://doi.org/10.1063/1.5029058

Suryanarayana, C., Norton, M. G. Practical Aspects of X-Ray Diffraction. In: X-Ray Diffraction. Springer **1998**, 63-94. https://doi.org/10.1007/978-1-4899-0148-4_3

Suzuki, V. Y.; Amorin, L. H. C.; Lima, N. M.; Machado, E. G.; Carvalho, P. E.; Castro, S. B. R.; Alves, C. C. S.; Carli, A. P.; Li, M. S.; Longo, E.; La Porta, F. A. Characterization of the Structural, Optical, Photocatalytic and: In Vitro and in Vivo Anti-Inflammatory Properties of Mn2+ Doped Zn2GeO4 Nanorods. *J. Mater. Chem. C* **2019a**, *7* (27), 8216-8225. https://doi.org/10.1039/c9tc01189g

Suzuki, V. Y.; Paula, N. H.; Gonçalves, R.; Li, M. S.; Pereira, E. C.; Longo, E.; La Porta, F. A. Exploring Effects of Microwave-Assisted Thermal Annealing on Optical Properties of Zn2GeO4 Nanostructured Films. *Mater. Sci. Eng. B Solid-State Mater. Adv. Technol.* **2019b**, *246*, 7-12. https://doi.org/10.1016/j.mseb.2019.05.023

Suzuki, V. Y.; Amorin, L. H. C.; de Paula, N. H.; Albuquerque, A. R.; Li, M. S.; Sambrano, J. R.; Longo, E.; La Porta, F. A. New Insights into the Nature of the Bandgap of CuGeO3 Nanofibers: Synthesis, Electronic Structure, and Optical and Photocatalytic Properties. *Mater. Today Commun.* **2021**, 26, 101701. https://doi.org/10.1016/j.mtcomm.2020.101701

Talapin, D. V; Mekis, I.; Go, S.; Kornowski, A.; Benson, O.; Weller, H. CdSe/CdS/ZnS and CdSe/ZnSe/ZnS Core-Shell-Shell Nanocrystals. *J. Phys. Chem. B* **2004**, *108* (49), 18826-18831. https://doi.org/10.1021/jp046481g

Talapin, D. V.; Lee, J. S.; Kovalenko, M. V.; Shevchenko, E. V. Prospects of Colloidal Nanocrystals for Electronic and Optoelectronic Applications. *Chem. Rev.* **2010**, *110* (1), 389-458. https://doi.org/10.1021/cr900137k

Wang, X.; Shi, J.; Feng, Z.; Li, M.; Li, C. Visible Emission Characteristics from Different Defects of ZnS Nanocrystals. *Phys. Chem. Chem. Phys.* **2011**, *13* (10), 4715-4723. https://doi.org/10.1039/c0cp01620a

Wang, P.; Wu, Z.; Wu, M.; Wei, J.; Sun, Y.; Zhao, Z. All-Solution-Processed, Highly Efficient and Stable Green Light-Emitting Devices Based on Zn-Doped CsPbBr3/ZnS Heterojunction Quantum Dots. *J. Mater. Sci.* **2021**, *56* (6), 4161-4171. https://doi.org/10.1007/s10853-020-05527-0

Xiao, J.; Song, C.; Song, M.; Dong, W.; Li, C.; Yin, Y. Preparation and Gas Sensing Properties of Hollow ZnS Microspheres. *J. Nanosci. Nanotechnol.* **2016**, *16* (3), 3026-3029. https://doi.org/10.1166/jnn.2016.10765

Yoffe, A. D. Semiconductor Quantum Dots and Related Systems: Electronic, Optical, Luminescence and Related

Eclética Química Journal, vol. 47, n. 3, 2022, 17-31
ISSN: 1678-4618
DOI: 10.26850/1678-4618eqj.v47.3.2022.p17-31

Properties of Low Dimensional Systems. *Adv. Phys.* **2001**, *50* (1), 1-208. https://doi.org/10.1080/00018730010006608

Zhang, Y.; Zhang, N.; Tang, Z. R.; Xu, Y. J. Graphene Transforms Wide Band Gap ZnS to a Visible Light Photocatalyst. the New Role of Graphene as a Macromolecular Photosensitizer. *ACS Nano* **2012**, *6* (11), 9777-9789. https://doi.org/10.1021/nn304154s

Zhang, Z.; She, J.; Chen, H.; Deng, S.; Xu, N. Laser-Induced Doping and Fine Patterning of Massively Prepared Luminescent ZnS Nanospheres. *J. Mater. Chem. C* **2013**, *1* (32), 4970-4978. https://doi.org/10.1039/c3tc30714j

Ziegler, B. J.; Xu, S.; Kucur, E.; Meister, F.; Batentschuk, M.; Gindele, F.; Nann, T. Silica-Coated InP/ZnS Nanocrystals as Converter Material in White LEDs. *Adv. Mater.* **2008**, *20* (21), 4068-4073. https://doi.org/10.1002/adma.200800724

Eclética Química Journal, vol. 47, n. 3, 2022, 17-31
ISSN: 1678-4618
DOI: 10.26850/1678-4618eqj.v47.3.2022.p17-31